Full Length Article

Atomizing high-viscosity non-Newtonian fluids with the ACLR nozzle: Correlation between internal flow and external spray instabilities

Miguel Ángel Ballesteros Martínez [*] , Prithika Roy , Juan Nicolás Solano Alarcón , Volker Gaukel

Institute of Process Engineering in Life Sciences: Food Process Engineering, Karlsruhe Institute of Technology, Kaiserstraße 12, 76131 Karlsruhe, Germany

ABSTRACT

Spray drying is a widely used method for producing food powders in large quantities, but it also has a high energy demand. To address this, one can increase the solid content of liquid feeds, although this, in turn, poses the challenge of atomizing high-viscosity liquids into fine droplets. The Air-Core-Liquid-Ring (ACLR) nozzle offers a potential solution for the atomization by inducing air and creating an annular flow inside the nozzle. Nevertheless, a challenge of this design is that it tends to present internal instabilities. This study investigates how feed viscosities up to 3 Pa·s, and feed dry-matter contents up to 57 % wt., influence the internal flow conditions and the resulting spray performance, i.e., the droplet size distribution and the spray angle. The results show that, while internal instabilities increment with increasing viscosities, the ACLR can seemingly achieve atomization with viscosities as high as 3 Pa·s, even at, compared to pressure swirl nozzles, low pressures (7 bar) and low air-to-liquid mass ratios (0.8). Nonetheless, a fraction of droplets over 500 μm remains, which needs to be addressed through higher ALRs or a geometrical optimization of the nozzle, before the nozzle can be considered for industrial applications. Additionally, we showed that the internal flow and the external spray instabilities can be correlated with each other. This confirms that any future studies attempting to increase the spray stability of the ACLR nozzle can focus on only one of these factors, and reasonably expect that the others will also improve.

1. Introduction

Drying processes are known to be the most energy-consuming type of unit operation in the food industry [1,2]. An EU-Project showed that 12–25 % of the total industrial energy consumption in many developed countries can be attributed to industrial drying [3]. In the field of food powders, most products available on the market are produced using a spray dryer [1]. Unfortunately, the potential for waste heat recovery is restricted with this type of process [4]. Additionally, the capacity of a spray dryer is limited by its specific water evaporation rate [5]. That is why increasing the dry-matter content of a liquid that is fed to the spray dryer is one of the most straightforward ways to both reduce energy consumption and increase production throughput. However, the effects of a high dry-matter content on the resulting powder morphology, rehydration capacity and flowability must also be taken into account. According to a model calculation on industrial spray drying by Fox et al. [1], an increase in feed dry matter content by 1 % could lead to a

decrease in thermal energy consumption of the spray dryer by 3.8 % or an increase in powder production capacity of 4.5 %.

The major drawback of increasing the feed dry-matter content is that it is linked with a sharp increase of the liquid viscosity, which causes complications in the atomization step [5] when a certain viscosity is exceeded. Consequently, it is vital that an appropriate nozzle design is selected that can handle those high viscosities. One promising nozzle design is the Air-Core-Liquid-Ring (ACLR) nozzle, which is a type of internal-mixing pneumatic nozzle [6]. The working principle of the ACLR nozzle is based on injecting a high-speed gas flow at the center of a flowing liquid feed. This favors the development of an annular flow inside the nozzle, with an air core surrounded by a liquid film, also called a liquid lamella.

The two-phase flow inside the nozzle allows it to handle liquids with higher viscosities than pressure swirl nozzles. For feed viscosities above 0.03 Pa•s, pressure swirl nozzles require high operating pressures (5–25 MPa [7]) just to atomize the liquid, which can easily become a limiting
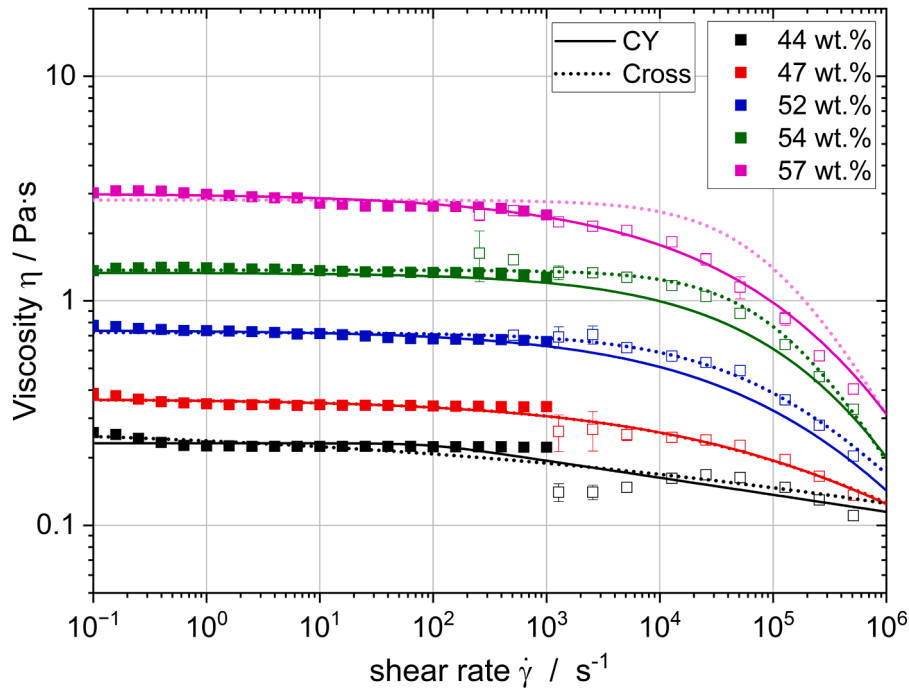
---

* Corresponding author.
  E-mail address: miguel.ballesteros@kit.edu (M.Á. Ballesteros Martínez).

Fig. 1. Viscosity of the maltodextrin solutions with different mass fractions. Full symbols represent data from a rotational rheometer, while empty symbols represent data from a capillary rheometer. The lines correspond to the regressions done using the Cross (dotted) and Carreau-Yasuda (continuous) models.

factor. In comparison, the ACLR has been shown to effectively handle viscosities ten times as high while only requiring pressures of 0.04–0.08 MPa [6]. Additionally, because the gas and liquid flows are combined inside the nozzle [8], lower gas flowrates are possible in internal-mixing atomizers, like the ACLR, in comparison to external-mixing atomizers [9]. For example, Stähle et al. [10] showed than an internal-mixing nozzle, in that case, an effervescent nozzle, requires only 30–50 % of the gas mass flowrate of external-mixing ones to achieve similar Sauter mean diameters (SMD). A lower atomizing gas flowrate leads to reduced operating costs should lead to a higher heat transfer efficiency inside the drying tower. The higher heat transfer is linked to the fact that: the lower the flowrate of the compressed gas, the lesser the cooling effect of the atomizing gas, which expands and cools down as it exits the nozzle, on the drying air current. Consequently, the lower the atomizing gas flowrate, the larger the temperature difference between the droplets and the drying air, leading to a higher heat transfer efficiency [11]. Based on these advantages, Wittner et al. [5] estimated that the ACLR nozzle can potentially reduce total energy consumption in a spray-drying process up to 29 % compared to a process using a standard pressure swirl nozzle, which is the most common type of atomizer utilized in the spray drying of foods [12].

Nonetheless, further investigation is needed, before the ACLR nozzle can fulfill its energy-saving potential. The existing studies on the ACLR have been restricted to viscosities from 0.03 to 0.39 Pa•s and dry-matter contents up to 47 % wt. [6,13], but so far no published attempt has been done to determine the upper limit of the feed dry-matter content and/or the feed viscosity. This is compounded by the fact that mixtures with dry-matter content above 30–40 % wt. tend to present an increasingly non-Newtonian, typically a shear-thinning, rheological behavior [14]. To maximize energy savings, we investigated how the nozzle performs at higher dry-matter contents. In addition, we investigated which critical parameters can be used to quantify and evaluate the nozzle performance.

Besides this, the ACLR nozzle is known to suffer from internal flow instabilities, which becomes more significant at high viscosities. This leads to an increase of the temporal unsteadiness of the droplet size distribution (DSD) and the SMD [13]. To understand the development of

these instabilities we investigated how they develop along the nozzle and along the general atomization process. In detail, we investigated the spray inside the nozzle itself, at the spray cone near the nozzle exit, and in the resulting spray droplets. This led to three variables chosen to evaluate nozzle performance: the lamella thickness inside the nozzle, the angle of the spray cone, and the DSD of the resulting spray. Correlating the temporal instabilities of the lamella, the spray cone and the DSD has another advantage. If the temporal variations could be proven to be all directly correlated, then any factor that reduces the unsteadiness in one of these can be reasonably expected to reduce the unsteadiness of the other ones. This would be useful, for example, for computational studies attempting to improve nozzle performance. In this case only part of the atomizing process, such as the internal flow, needs to be simulated, strongly reducing the computational time. It would also be useful for future experimental analysis, or for industrial testing, since it means that the temporal unsteadiness can be monitored simply by observing the external spray and not also the internal flow. This would mean that the nozzle would no longer need to be constructed out of transparent materials.

With that in mind, this study encompasses two complementing objectives. On the one hand, to expand the knowledge on the ACLR nozzle for higher viscosities, assessing how well this nozzle concept can atomize shear-thinning feeds with a dry-matter content of up to 57 % wt. and viscosities up to 3 Pa·s (measured at 10^3 s^{-1}). On the other hand, to build on the insights of our previous work [15], we evaluated how the high viscosities affect the internal flow instabilities of the nozzle and, in turn, how these instabilities correlate with the spray stability and the width of the DSD.

1.1. Model solutions

The experiments were carried out with aqueous solutions of maltodextrin C*DryTM MD 01,958 (dextrose equivalent = 8.8, Cargill Deutschland GmbH, Düsseldorf, Germany). In total, five different solutions were produced, with dry-matter contents between 44 and 57 % wt. Only the solutions from 52 % wt. and higher were actually considered for the performance analysis (see Section 5) in this study, since

Table 1

Correlation parameter (R^2) for the Cross and Carreau-Yasuda (CY) models.

Dry-matter content [% wt.]	Cross R^2 [-]	Carreau-Yasuda R^2 [-]
45	0.79	0.81
47	0.94	0.94
52	0.97	0.95
54	0.95	0.92
57	0.93	0.99

Table 2

Maximum (max), minimum (min), and range of variation (var) of the liquid volume flow (Q_L) for the non-Newtonian MD solutions. The zero viscosity is mentioned for reference.

Dry-matter content [% wt.]	η_0 [Pa·s]	Q_{Lmin} [L·h^{-1}]	Q_{Lmax} [L·h^{-1}]	Q_{Lvar} [L·h^{-1}]
44	0.23	20	60	±1
47	0.37	20	60	±1
52	0.74	20	25	±2
54	1.33	14	16	±2
57	3.01	10	10	2–12[a]

[a] The flowrate tended to vary around 10 ± 2 L·h^{-1} for a couple seconds but would suddenly decrease to 2 L·h^{-1}, then return to 10 L·h^{-1}.

Table 3

Process conditions evaluated. The ALR is given for each of the pressures (0.2–0.7 MPa) used in the experiments.

Dry-matter content [% wt.]	η_0 [Pa·s]	Nominal flowrate [L·h^{-1}]	ALR [-]			
			0.2 MPa	0.4 MPa	0.6 MPa	0.7 MPa
52	0.74	20	0.05	0.11	0.14	0.23
54	1.33	16	0.08	0.22	0.35	0.42
57	3.01	10	0.18	0.35	0.68	0.77

maltodextrin (MD) fractions up to 47 % wt. have already evaluated by Wittner et al. [13]. Nonetheless, all five mixtures were included in the analysis of the rheological behavior shown in this chapter, as well as in the analysis of the pump performance of next chapter (see Table 2). This was done to illustrate how these two factors were affected by the higher maltodextrin content utilized in this study in comparison to previous works.

The viscosities of the MD solutions were measured with a rotational rheometer (Physica MCR 301, Geometry DG26.7, Anton Paar, Graz, Austria) at shear rates between 1 and 10^3 s^{-1}. To illustrate the non-Newtonian behavior, the measurements were complemented with measurements from a capillary rheometer Rheograph 6000 (GÖTTFERT Werkstoff-Prüfmaschinen GmbH, Buchen, Germany), at shear rates between 10^3 and 10^6 s^{-1}. The complete viscosity profiles for the maltodextrin solutions are shown in Fig. 1. A strong shear-thinning behavior can be seen for all solutions. In general, the rotational and capillary measurements overlap well. There is a noticeable jump between the data of the two rheometers for the least viscous solution.

To characterize the shear-thinning behavior, we fitted the rheological measurements with two different options of non-Newtonian models: the Carreau-Yasuda (CY) model [16,17] and the Cross model [18]. These options were selected because they are commonly used to characterized shear-thinning fluids [19]. Additionally, they are available in simulation tools like STAR-CCM+ [20] or ANSYS Fluent [21], which would make this characterization useful for future numerical studies. Given that our current research on the ACLR nozzle is partly numerical [22], it was particularly important that the rheological model we fitted could later be implemented in numerical studies. For the CY model, the equation is the following:

$$\eta(\dot{\gamma}) = \eta_\infty + (\eta_0 - \eta_\infty)(1 + (\lambda \cdot \dot{\gamma})^a)^{(n-1)/a} \qquad (1)$$

where η is the viscosity, η_0 is the zero viscosity, η_∞, the viscosity at infinite shear rate, and $\dot{\gamma}$ is the shear rate. The correlation parameters are the relaxation time λ, the power index n, and the parameter a, which control the shear-thinning behavior. For the Cross model, there is a quite similar equation:

$$\eta(\dot{\gamma}) = \eta_\infty + (\eta_0 - \eta_\infty)(1 + (\dot{\gamma}/\dot{\gamma}_c)^m)^{-1} \qquad (2)$$

where $\dot{\gamma}_c$ is the critical shear rate, at which shear-thinning begins to occur. In this case, the correlation parameter m controls the shear-thinning behavior. As it can be noticed, the main difference between the two models is that CY has three degrees of freedom to fit the shear-thinning behavior (λ, n and a), while the Cross model only has two: $\dot{\gamma}_c$ and m. The fitting curves for both models are shown in Fig. 1.

The correlation coefficients R^2 for both models are shown in Table 1, and the corresponding model parameters are shown in Appendix A. In general, both models perform similarly. The most important range of comparison was for the shear rates around $10^5 - 5 \times 10^5$ s^{-1}, since this is the range of the shear rates that can be expected, at least based on the simulations from our previous numerical study [22]. The Cross model fits the data slightly better at 52 % and 54 %, while the CY model provides a better fit for 57 %. Given that both models have similar performances, the choice of which to use in future simulations is somewhat arbitrary.

1.2. Experimental setup

All measurements were carried out in our spray test rig, which has been described in detail, and with schematics, in a previous work [23]. In short, it is composed of a closed cabin with a vertical atomizer on top. The liquid flow is supplied by an eccentric screw pump and measured by a gear flow meter. The air is supplied by a compressor and the air pressure is adjusted with a pressure regulator, and its resulting volume flow is measured by a gas flow meter.

It has to be mentioned that adjusting the liquid volume flow became increasingly difficult as the viscosity increased. This is most likely related to the fact, that the pump used was only designed for viscosities up to 1 Pa·s. To illustrate this limitation, Table 2 shows the minimum and maximum flow rates that the pump could achieve for different viscosities, as well as the estimated variation of the value read on the gear flow meter. Even with a viscosity of 0.74 Pa·s, the maximum flow rate was severely limited. The operation range became even smaller with higher viscosities, and the flow variation increased significantly. By 57 % wt. MD, controlling the flowrate was no longer possible.

It should be kept in mind that most of the measurements were carried out at very short spans of time (see Section 4), usually 0.1–1 s. The measuring frequency of each method was also very high, between 10 and 20 kHz. In comparison, the pump has a speed of 5 Hz. On one hand, this means that the flowrate fluctuations should not affect the measured data, because the measurements happen quickly in comparison to the pump oscillations, and they were conducted at moments were the nominal flowrate (shown in Table 3) was reached. An exemption to this is the droplet size measurements performed at 1 Hz (see Section 4.3). In that case, the effect of the pump can be considered as one of the causes of the standard deviations seen in the DSD (see Section 5.3). On the other hand, the short measuring time also means that the exact effect of the pump oscillations could not be quantified during the instability frequency analysis. This is because the effective resolution of the frequency analysis, as it is explained in Section 4.4, was 1 Hz, which is very close to the actual speed of the pump. Consequently, the influence of the pump oscillations could not be decoupled from the flow and spray instabilities.

1.3. Characterization of flow and spray instabilities

The spray temporal stability was analyzed at three different sections of the atomization process: the annular flow inside the nozzle (see
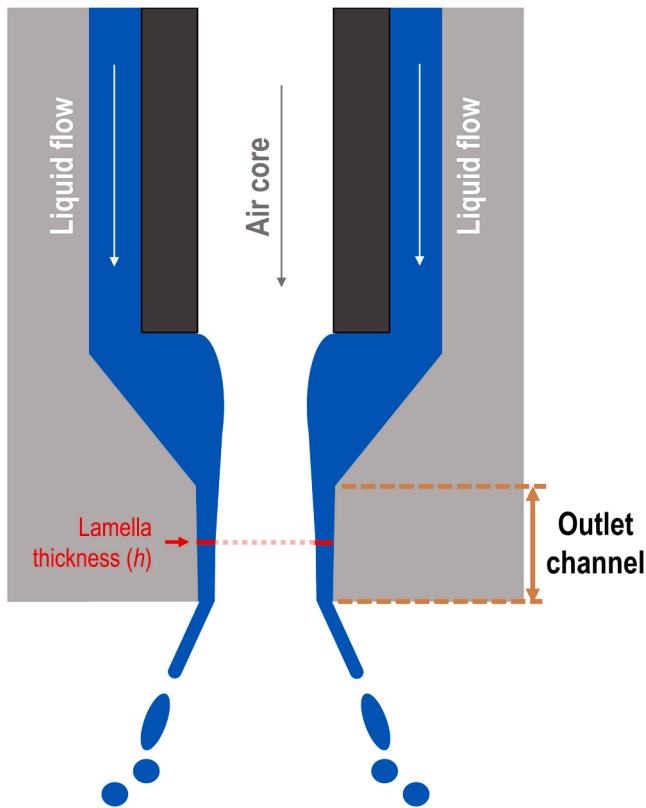
Fig. 2. Schematic of the Air-Core-Liquid-Ring (ACLR) nozzle. Adapted from Ballesteros Martinez and Gaukel [1]. The red line indicates where the lamella thickness is measured inside the nozzle.

Section 4.1), the spray cone that forms at the nozzle exit (see Section 4.2), and the spray droplet size (see Section 4.3). The instabilities that occurred in each of the three sections were then correlated with each other using a Fourier transformation (see Section 4.4). As mentioned while discussing the model solutions, these measurements were only realized for the three maltodextrin solutions with a mass fraction of 52 % wt. or higher. Each mixture was also atomized at four different pressures. The different conditions analyzed are shown in Table 3, along with the air-to-liquid mass ratio (ALR), for reference. For each malto-dextrin solution, a fixed volume flowrate was used. The difference between the flowrates is a consequence of the limitations mentioned in Section 3.

1.4. Lamella thickness inside the nozzle

To characterize the internal flow instabilities, we determined the thickness of the liquid film, i.e. lamella, of the annular flow that develops inside the nozzle. To exemplify this, Fig. 2 shows a schematic of the nozzle design. As it can be seen, the ACLR nozzle is composed of an outer casing, where the liquid flows, and an internal capillary that injects the gas. The outer casing was constructed with clear acrylic, which allows the direct optical visualization of the flow conditions inside the outlet channel of the nozzle. A high-speed video camera (OS3-V3-S3, Integrated Design Tools Inc., Tallahassee, FL, USA) recorded the internal flow at a framerate of 20 kHz. Each measurement was composed of 10,000 images, which amounts of 0.5 s measurement time. The exposure time of each image was 5 μs, and the resolution was around 10 μm/pixel. The images were processed with a Matlab (The MathWorks Inc., Natick, MA, USA) code to measure the thickness of the liquid film, i.e. lamella, inside the nozzle. This lamella thickness was measured at the middle of the outlet channel, indicated in Fig. 2 as the dotted red line. The lamella thickness at the left and right sides of the channel were determined separately. The algorithm of the code, and more details about the measuring method, is described in Wittner et al. [13], who first developed the setup to measure the lamella thickness inside the ACLR nozzle.

In order to characterize the unsteadiness of the internal flow, we continuously tracked how the lamella thickness (h) changed with time. To statistically characterize the lamella thickness variation, the 5 %, 50 % and 95 % percentiles, which are denoted as $h_{5,0}$, $h_{50,0}$, and $h_{95,0}$, respectively, were calculated for each combination of pressure and viscosity. The data collected from the left and the right side of the channel were treated as a single group of measurements for the calculation of the percentiles.

1.5. Spray cone angle

Characterizing the external flow instabilities presented the challenge that the ACLR nozzle does not produce a continuous conical liquid sheet, as seen commonly in pressure swirl nozzles [7], but rather a set of irregular and partly disconnected liquid ligaments. An example of the spray obtained near the nozzle outlet is shown in Fig. 3. Nonetheless, we had to define a single parameter that represented the stability of the spray pattern. For that purpose, we defined a spray cone angle, which works as the angle of an imaginary cone that encompasses most of the ligaments observed near the nozzle outlet.

The process of determining this angle begins by recording the spray pattern using the same setup as the one for the lamella thickness, although, in this case, the spray is captured at a recording speed of 10 kHz. The camera was focused about 5 mm below the center of the outlet orifice, capturing an atomization area of approximately 11×11 mm. Previous angle measurement experiments have been performed at this distance, making it suitable for this study [24]. Within one
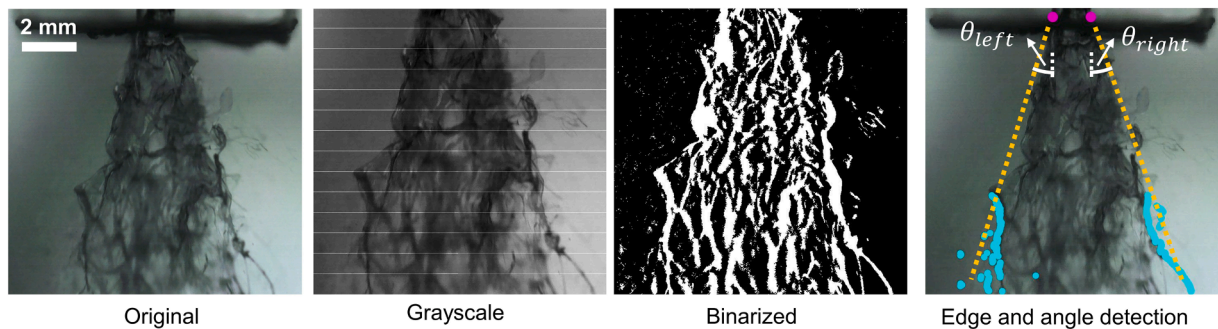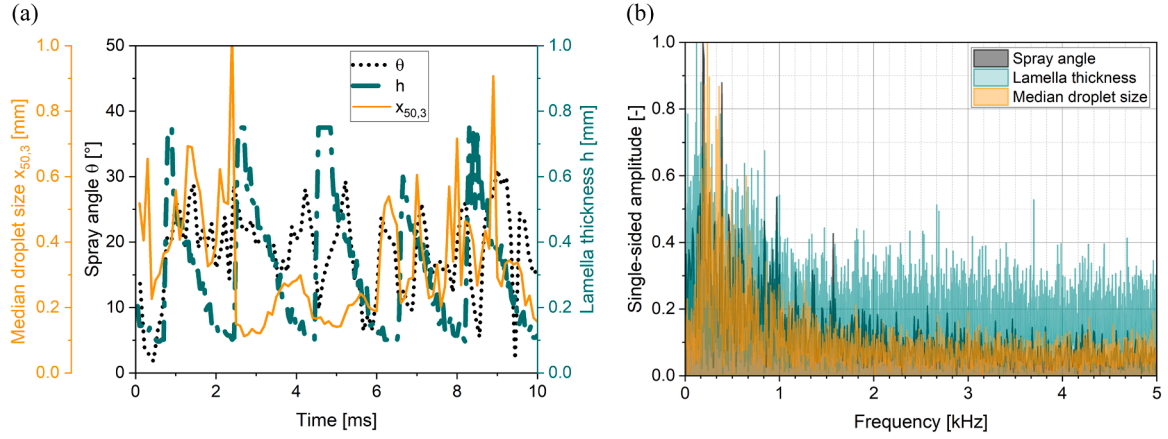

Fig. 3. Sample image of the first atomization area at the nozzle outlet (MD = 54 % wt., ALR = 0.35) and how the image looks after the different stages of post-processing. The grayscale image has been simplified by reducing the horizontal division to just 14 stripes for visualization purposes. The angle detection process is indicated on the last image on the right.

(a) (b)

Fig. 4. (a) Example of the time-domain measurements of the spray angle, the lamella thickness and the median droplet size. The measurements were taken at 0.2 MPa, with a flowrate of 16 L·h^{-1} and for the MD solution of 54 % wt. (b) Corresponding single-sided amplitude spectrum that results from the FFT analysis. The identified dominant frequencies are shown in Table 5.

measurement, 1000 images were taken at a frame rate of 10 kHz, resulting in a measurement time of 0.1 s. The exposure time was 2 μs.

Each of the images captured by the camera was processed using a code implemented in MATLAB. To make the principle of the algorithm clearer, Fig. 3 shows a sample image in the different stages of processing. The first step was to convert the 16-bit RGB image into 8-bit grayscale, split it in half vertically and then separate it horizontally into 50 strips of pixels. The saturation of the pixels of each strip was then locally enhanced to increase the contrast between the liquid ligaments and the background. The enhanced image is the one shown as grayscale in Fig. 3. In the next step, the image was binarized with a sensitivity threshold of 0.55. The various strips of the decomposed image were then concatenated back together, as can be seen in the binarized image in Fig. 3. After this, the edge of the spray cone was determined on the left and right side of the image, particularly on the bottom third part of the image. We only considered the bottom part of the image based on some pre-testing with the algorithm, because otherwise the angle calculation was too sensitive to small changes in the pixels detected at the spray edge. To eliminate some of the noise from the background, separated ligaments that were smaller than 3 pixels, which corresponds to 38 μm, were not considered for the edge detection. The detected edge can be seen as the blue edge points on the right image in Fig. 3.

Once the edge was defined, we calculated two half-angles, one for each side of the image. For that purpose, lines were drawn from the nozzle outlet (shown in Fig. 3 as the two purple dots) to each edge pixel, that is, the pixels marked in blue. For each side of the image, a distribution was computed for the angles corresponding to all drawn lines. The 90 % percentile of the resulting angle distribution was determined, and it was used as the half-angle for the corresponding side. The two half angles are illustrated in the photo in Fig. 3 as θ_{left} and θ_{right}. We chose 90 % because it ensured that most of the ligaments were included inside the defined spray cone, but that random flying ligaments or errors in the binarization would not artificially inflate the calculated value. The two half-angles were added up to determine the spray angle, θ, for the specific image. With this process, a single θ was determined for each image taken.

1.6. Droplet size characterization

Droplet size measurements were performed using a laser diffraction spectroscope (Spraytec, Malvern Instruments, Malvern, UK). It was equipped with a 750 mm focal lens, offering a droplet size measuring range of 2–2000 μm. Previous studies on the ACLR nozzle placed the spectrometer usually 25 cm [13,25], but we increased this distance to 35 cm because of the high viscosity of the liquids utilized in this

investigation. To confirm if the distance was sufficient, we recorded the spray pattern that the nozzle produced up to 10 cm below the nozzle exit. The purpose was to ensure that all liquid ligaments break up into spherical droplets before they reach the laser. More details about how this was evaluated can be found in Appendix B. The laser beam crossed the full cone spray angle at the nozzle axis centerline. Two types of measurements were carried out for each evaluated condition. First, a continuous measurement was performed over 2 min with a measurement frequency of 1 Hz. The purpose of this was to obtain an average distribution of the droplet sizes that the atomizer produces, over a large span of time. Second, a rapid measurement was conducted at a frequency of 10 kHz over a time of 1 s, leading to 10,000 DSDs. This would provide information about the DSD fluctuation and determine its temporal unsteadiness. Each recorded distribution had to be corrected from the beam-steering effect. This effect is a systematic error that causes the apparent detection of large spray droplets due to density gradients in the gas phase, and it is especially prevalent in pneumatic nozzles [26]. The correction was done by adapting the code developed by Wittner et al. [27]. In order to characterize the unsteadiness of the spray droplets, we tracked the 10 %, 50 % and 90 % volumetric percentiles of the measured sizes, which are denoted as $x_{10,3}$, $x_{50,3}$, and $x_{90,3}$, respectively, as well as the Sauter Mean Diameter (SMD).

1.7. Correlation of temporal unsteadiness

A way to evidence that the different instabilities are directly correlated is to verify if they have matching oscillation frequencies. This is the purpose of the Fourier transform analysis. A Fourier transform analysis is a method to decompose an input signal, which is usually a function of time, t, into a combination of periodic functions of different frequencies, f. This effectively transforms the signal representation from the time domain to a frequency domain, which allows us to identify if the temporal oscillations of the measurement have a characteristic frequency or if they are simply caused by random noise [28]. For a continuous signal, the transform is defined as:

$$S\left(f\right) = \int_{-\infty}^{\infty} s(t)e^{-2\pi ift}dt \tag{3}$$

where $S(f)$ and $s(t)$ represent the signal in the frequency and the time domains, respectively. The complex exponential term, noted by the imaginary unit, $i = \sqrt{-1}$, describes the periodic function at each frequency [28].

However, the signal from an actual experimental measurement is neither continuous nor infinite. Instruments take measurements at
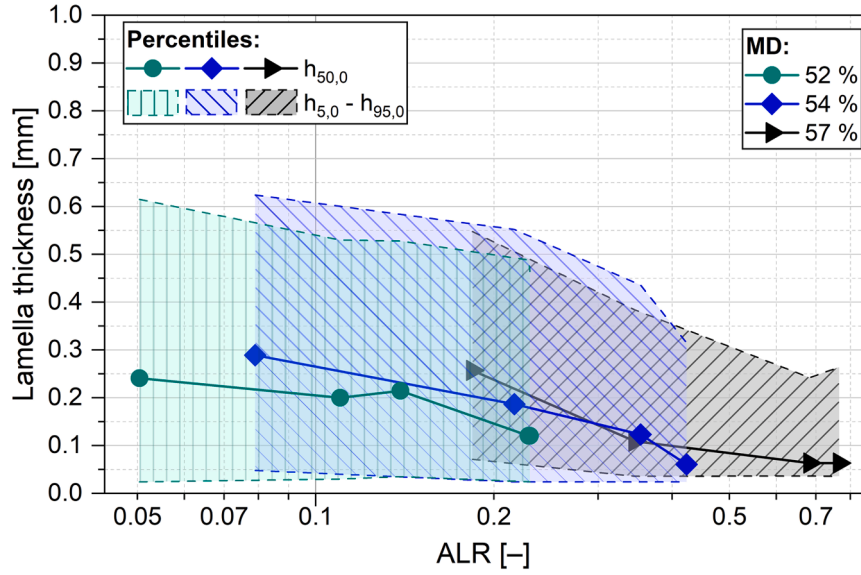
Fig. 5. Lamella thicknesses of different maltodextrin (MD) mass fractions (indicated with the different colors and markers) at increasing ALRs. The median ($h_{50,0}$) is indicated by full symbols connected by lines. The 5 % and 95 % percentiles ($h_{5,0}$ and $h_{95,0}$) are indicated as the shaded regions.

discrete, and usually regular, intervals, and for a finite time period. On top of that, the resulting signal is usually computed numerically rather than analytically, using numerical algorithms. With this in mind, the discrete Fourier transform (DFT) is usually used to transform data into the frequency domain. The fundamental equation of DFT is similar to Eq. (3), but with a discrete series instead of an integral. For a discrete signal measured with a sampling rate Δt over a period of T, the DFT is:

$$\mathbf{S}[m\Delta f] = \Delta t \sum_{n=0}^{N-1} \mathbf{s}[n\Delta t] e^{-i(2\pi/N)mn} \tag{4}$$

where m and n represent the frequency and time indexes, respectively. N is then the length of the signal vector, which means that $N = T / \Delta t$. Δf, also known as the frequency resolution, represents the minimum difference between the discrete frequencies, is usually defined as $1 / T$. The DFT approach is considered valid until the evaluated frequency reaches half of the sampling rate [29]. Algebraically speaking, this means that $\mathbf{s}$ is a vector of the signal values in the time domain from 0 until $N\Delta t$, while $\mathbf{S}$ is the corresponding vector of signal values in the frequency domain from Δf until $N\Delta f/2$. For this specific study, this means that the frequency analysis encompassed frequencies between 1 and either 5 kHz (for the spray angle and droplet sizes) or 10 kHz (for the lamella thickness). However, for the analysis to be reliable, the frequencies to be identified should ideally not be close to either of the two boundaries [30]. This is the reason why the actual effect of the pump oscillation could not be elucidated in this study, since the pump speed (5 Hz) is fairly close to the lower frequency limit. The solution to this would be to increase T, which could be addressed in future work.

One limitation of the DFT approach is that its required computational time scales with N^2, which can quickly become problematic for large datasets. Therefore, we use a variation of the DFT, namely, the Fast Fourier Transform analysis (FFT) with the Cooley–Tukey algorithm [31]. In short, the algorithm recursively decomposes the DFT in halves, which reduces the computational time from scaling with N^2T to scaling with the $N\log_2 N$ [32].

Using this algorithm, we developed a data processing code in MATLAB, which imported the discrete time data for the various analyzed parameters: the spray angle, the lamella thickness, the SMD, as well as the $x_{50,3}$ and $x_{90,3}$ of the DSD. As an example, Fig. 4a shows 10 ms of each measurement in the time domain. It should be noted that the entire measurement period was longer and also different for each

analyzed parameter (See Sections 4.1–4.3). The code then uses the FFT to transform the signals into the frequency domain. The result is shown in Fig. 4b. Then, the code identifies the most dominant frequency for each signal, i. e., the signal with the greatest power/amplitude.

The dominant frequencies of every parameter were then determined, so that the internal, external and DSD instabilities could be matched. Following the usual breakup model for a conical spray [33], instabilities first develop in the liquid lamella, grow along the spray cone and then lead to the droplet formation. Consequently, the oscillation frequency of the lamella thickness was considered the reference value, and the oscillation frequencies of the other parameters were compared against it to establish if they matched in value. To account for possible experimental uncertainty, two frequencies were considered to match if their values were ±50 Hz near each other. Additionally, we also signaled frequencies that were up to ±200 Hz near the reference value, to highlight frequencies that are similar but not matching the lamella instabilities. These threshold values were chosen because the FFT analysis, as mentioned before, can result in dominant frequencies ranging anywhere between 1 Hz and 5 kHz (or 10 kHz for the lamella thickness), which means that ±50 Hz represent at most 1 % of the possible range, and ±200 Hz represent at most 5 % of the possible range.

2. Results and discussion

As mentioned before, this work had two objectives: to evaluate the applicability of the ACLR for highly viscous feeds and to correlate the internal and external flow instabilities with the spray temporal unsteadiness. For that purpose, each of the flow and spray variables of interest was first analyzed separately (see Sections 5.1–5.3) and then the frequency of their oscillations were correlated using the FFT analysis (see Section 5.4).

2.1. Influence of high viscosity on the internal nozzle flow (lamella thickness)

Fig. 5 shows the lamella thickness for the three different solutions at different ALRs. The range of variation is illustrated as the shaded area between $h_{5,0}$ and $h_{95,0}$. The $h_{50,0}$ is also shown in the middle of the shaded area. The most evident observation from the experimental data is that all solutions, regardless of their very different viscosities, follow the same behavior with respect to the ALR. The lamella thickness for all
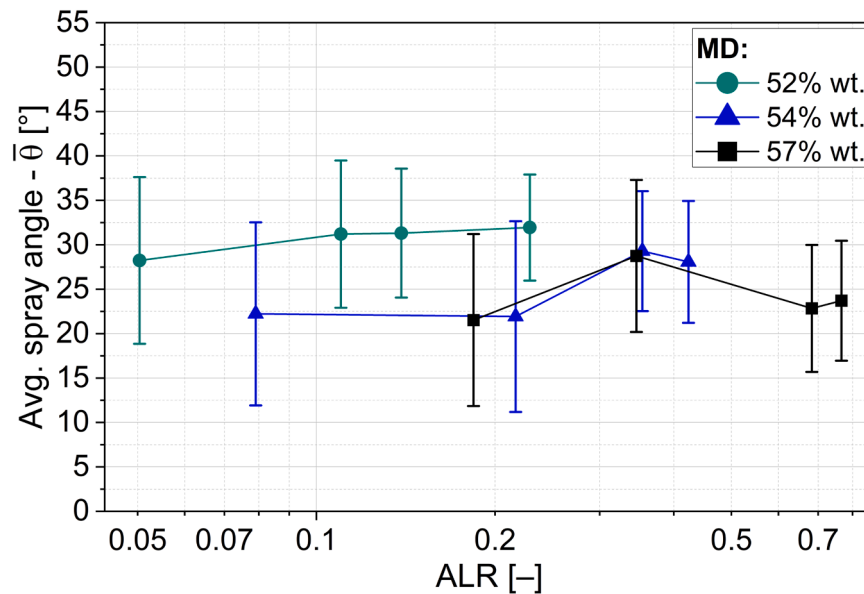
Fig. 6. Average spray angle of different maltodextrin (MD) mass fractions (indicated with the different colors and markers) at increasing ALRs. The error bars represent the standard deviation from the 1000 measurements taken for each point.
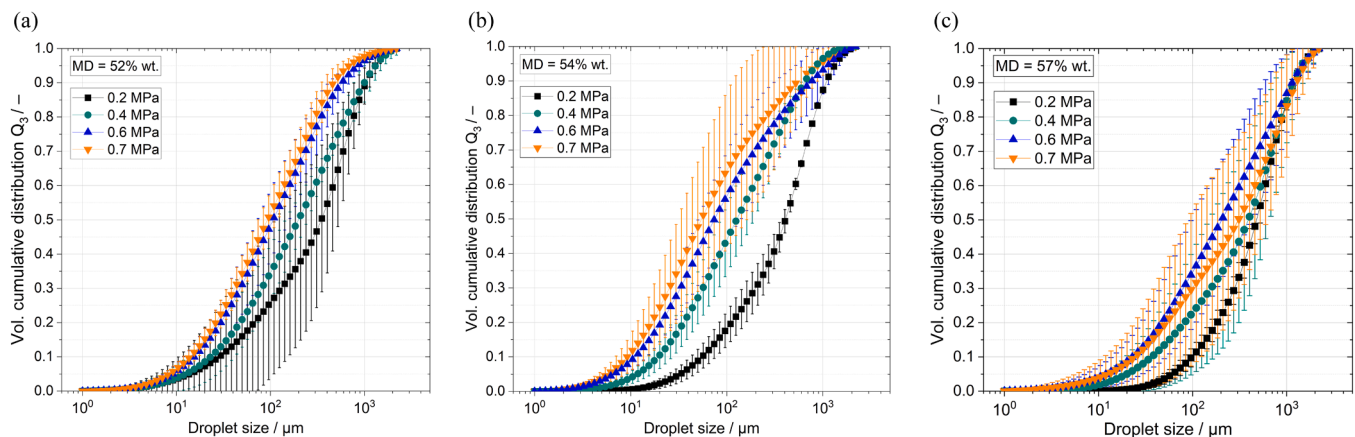
Fig. 7. Volumetric droplet size distributions at increasing pressures for the different maltodextrin (MD) fractions: (a) 52 % wt.; (a) 54 % wt.; and (a) 57 % wt. The error bars represent the standard deviation from all the distributions collected during the continuous measurement. The corresponding ALRs for each pressure, and MD fraction, is shown in Table 3.

solutions decreases with the ALR. In fact, it seems to share very similar values at similar ALRs, regardless of the viscosity. At first glance, this might seem to contrast with results from our previous study [15], which covered viscosities up to 0.34 Pa•s and where we concluded that higher viscosities required higher pressures, to achieve the same lamella thickness. Nonetheless, the previous study varied the air pressure at a constant volume flow for all MD mixtures, while this study compares the mixtures on the sole basis of the ALR. Comparing the results of both studies would only be meaningful if the analysis of the lamella had been done on the basis of the ALR for both. Regardless of this, the trend observed at these high viscosities is very promising for the process intensification possibilities of the ACLR, because it means that the annular flow can be produced even at high dry-matter fractions, while still maintaining ALRs below 1. To give a point of comparison, most studies with airblast nozzles, which are external-mixing atomizers, report ALRs between 1 and 15, regardless of whether they worked with viscosities of 2 mPa•s [34] or 1 Pa•s [35]. The main limitation would then be the pumpability of the liquid feed, to maintain stable volume flows.

2.2. Influence of high viscosity on the external flow (spray cone angle)

Fig. 6 shows the average spray angle measured for the different maltodextrin solution, at increasing ALRs. The average spray angles observed for these viscous mixtures range between 20 and 32°, which means that they are markedly smaller than the ones observed for lower viscosities, e.g. 35–50° for 0.14 Pa•s [15]. This could be expected, since viscosity acts as an opposing force to the disintegration of the lamella and the expansion of the spray cone. However, there is no clear tendency for the spray angle with the ALR, at least not one that can be generalized for all MD solutions. Only the 52 % wt. solution shows a slight but consistent increase in the spray angle as the ALR increases. On the other hand, the spray angles for 54 % wt. and 57 % wt. oscillate between 20°–30°.

Another important point to mention is the standard deviation, which is shown as the error bars in Fig. 6. As it can be noticed, the standard deviation tends to decrease as the ALR increases. This is consistent for all maltodextrin solutions, even though they have such different viscosities. The fact that the standard deviation of the spray angle and the range of variation of the internal lamella both decrease with higher ALRs
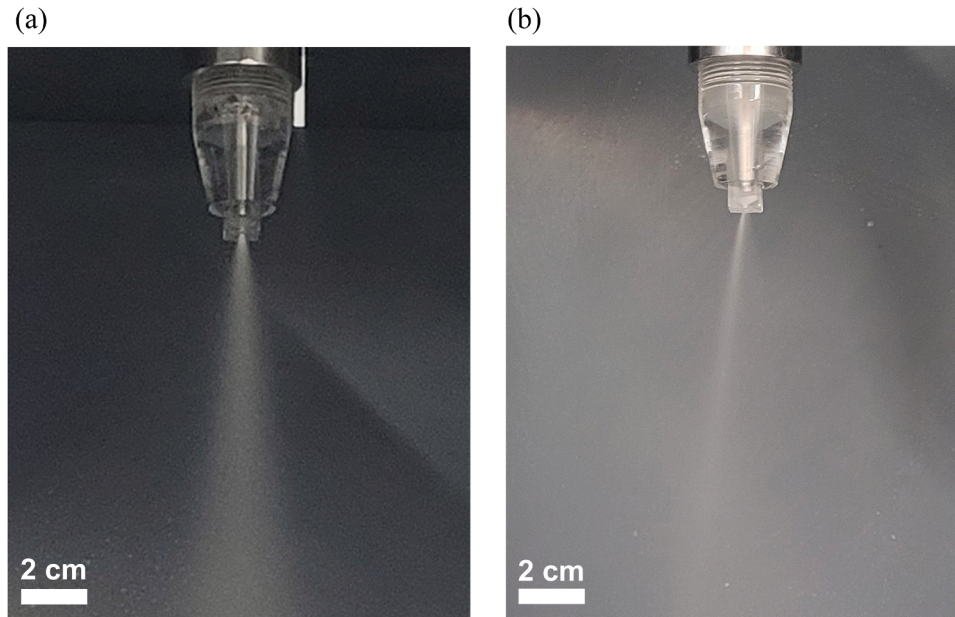
(a) (b)

Fig. 8. Spray formed at 0.4 MPa for (a) the 54 % wt. MD solution; (b) the 57 % wt. MD solution.
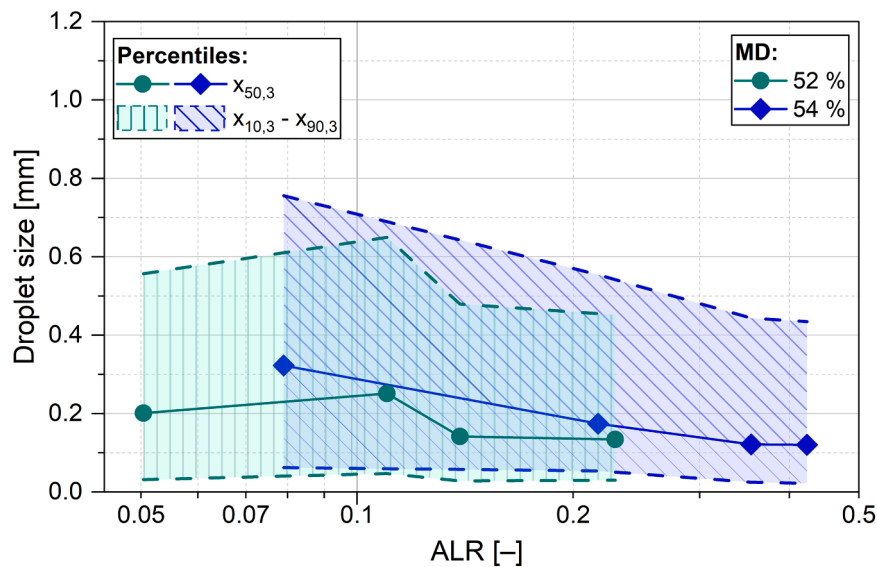

Fig. 9. Droplet size variation of two different maltodextrin (MD) mass fractions (indicated with the different colors and markers) at increasing ALRs. The volumetric median ($x_{50,3}$) is indicated by full symbols connected by lines. The 10 % and 90 % percentiles ($x_{10,3}$ and $x_{90,3}$) are indicated as the shaded regions.

Table 4
Sauter mean diameter (SMD), volumetric mean diameter ($\bar{x}_3$), range, and span for different MD mass fractions at increasing ALRs.

Dry-matter content [% wt.]	ALR [-]	SMD [mm]	$\bar{x}_3$ [mm]	Range [mm]	Span [-]
52	0.05	0.10	0.48	0.53	2.61
	0.11	0.13	0.40	0.60	2.39
	0.14	0.08	0.24	0.45	3.18
	0.23	0.07	0.20	0.42	3.14
54	0.08	0.19	0.54	0.69	2.15
	0.22	0.12	0.27	0.50	2.87
	0.35	0.09	0.26	0.42	3.44
	0.42	0.05	0.20	0.41	3.43

highlights the connection between the lamella and the spray cone. It is a sign that reducing the lamella instabilities should lead a more stable spray cone, even at these high viscosities. The choice to use the standard deviation in this case comes from the fact that the spray angle tended to oscillate symmetrically around its average value. This can be noticed in Fig. 4a. In comparison, the lamella thickness, also shown in Fig. 4a, has very clear narrow peaks, so the maximum values are much further apart from the median than the minimum values, which leads to the one-sided distributions seen in Fig. 5.

2.3. Influence of high viscosity on the droplet size distribution

As mentioned in Section 4.3, the DSD was measured with two different methodologies: a low-frequency measurement at 1 Hz over 2 min, and a rapid measurement at 10 kHz over 1 s. The low-frequency averaged DSDs are shown in Fig. 7, for all evaluated conditions. The
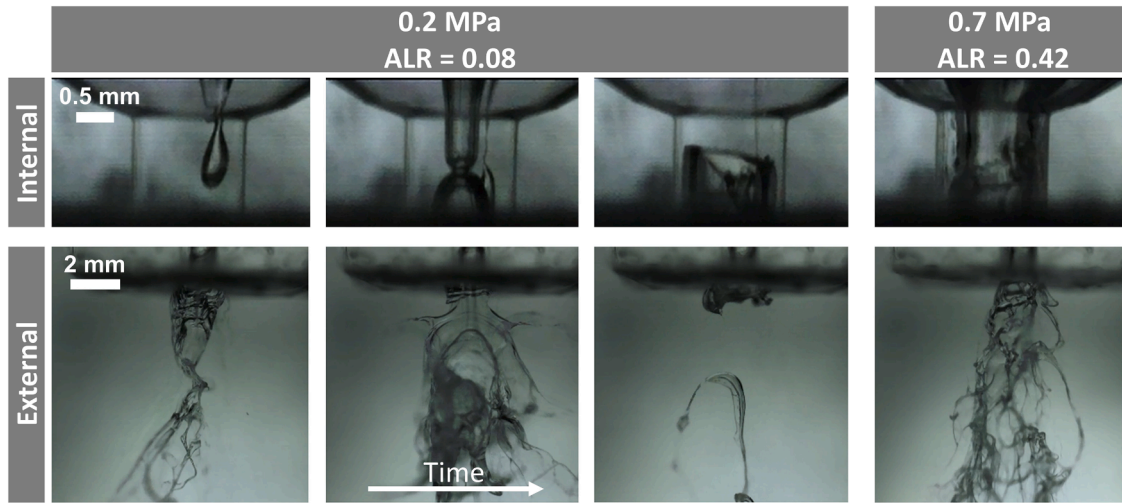
Fig. 10. Snapshots of the flow inside and right under the exit of the ACLR nozzle, for the 54 % wt. MD solution. Because of the pulsating nature of the flow at that pressure, multiple snapshots are provided for 0.2 MPa, organized sequentially in time. For 0.7 MPa, only one example snapshot, since the flow pattern remained stable across time.

Table 5

Dominant frequencies of the temporal unsteadiness for the lamella thickness, the spray angle, the $x_{50,3}$, and the $x_{90,3}$. No droplet size data could be collected for 57 % wt. Green underlined values are within ±50 Hz of the lamella thickness frequency. Orange italicized values are within ±200 Hz. The corresponding ALRs for each pressure, and MD fraction, is shown in Table 3.

MD [% wt.]	Pressure [MPa]	Dominant frequency [Hz]				
		Lamella thickness	Spray angle	SMD	$x_{50,3}$	$x_{90,3}$
52	0.2	**486**	*440*	1519	17	99
	0.4	**604**	*570*	185	*761*	375
	0.6	**108**	*300*	849	*251*	*62*
	0.7	**112**	*100*	3	*37*	200
54	0.2	**204**	*200*	3	*207*	53
	0.4	**88**	*80*	*92*	*115*	*72*
	0.6	**128**	*190*	1556	1487	*13*
	0.7	**412**	*310*	182	984	55
57	0.2	**280**	*296*	—	—	—
	0.4	**120**	*156*	—	—	—
	0.6	**33**	*44*	—	—	—
	0.7	**80**	*64*	—	—	—

Table 6

Fitting parameters of the Cross model for the non-Newtonian maltodextrin solutions.

| Dry-matter content [% wt.]	η_0 [Pa·s]	$\dot{\gamma}_c$ [s^{-1}]	M [-]
44	0.29	1.45	0.13
47	0.37	1.45	0.33
52	0.72	1.29	0.58
54	1.37	1.32	0.89
57	2.81	0.98	0.90

Table 7

Fitting parameters of the Carreau-Yasuda model for the non-Newtonian maltodextrin solutions.

Dry-matter content [% wt.]	η_0 [Pa·s]	λ [s]	N [-]	A [-]
44	0.23	10,425.09	0.92	2.16
47	0.37	2.09	0.59	0.31
52	0.74	1.03	0.10	0.38
54	1.33	0.49	−0.60	0.46
57	3.01	0.08	−1.22	0.35

first remark that must be made is that the distributions show that the ACLR nozzle can atomize liquids with viscosities as high as 3 Pa·s while requiring relatively low pressures and ALRs. Fig. 7c, for example, shows that around a third of the liquid feed can be turned to droplets below 100

μm, with only 0.7 MPa and an ALR of 0.8. Additionally, the DSD shifts to smaller sizes as the pressure, and with it the ALR, increases. This fits the expected behavior for a twin-fluid nozzle. The range of the shift to smaller sizes seems to decrease with higher viscosities. This is especially

(a)   (b)
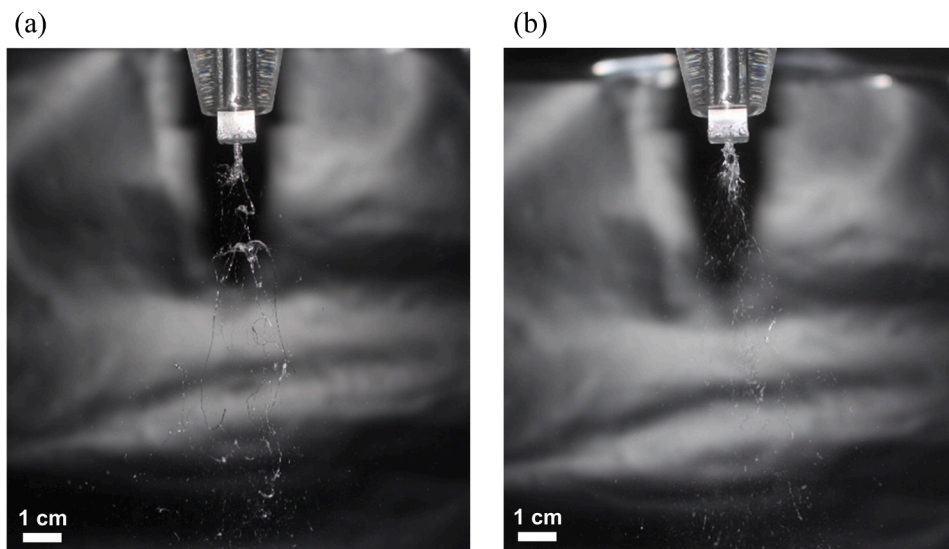
Fig. 11. Snapshots of the spray cone formed until 10 cm under the ACLR nozzle, for the 54 % wt. MD solution, at: (a) 0.2 MPa (ALR = 0.08); and (b) 0.7 MPa (ALR = 0.42).

evident when comparing 52 % and 57 % wt. (see Fig. 7a and 7c). The ALRs for 57 % wt. are consistently higher, yet still present larger droplet sizes.

Although it is promising to see that atomization is achieved, it can also be noticed that a high proportion of large droplets is observed and that there is a large variation of the DSD, which is clear from the standard deviations shown in Fig. 7. On the topic of the large standard deviations, they are mostly caused by the variation of the lamella thickness (see Fig. 5), but the pump flow variations (mentioned in Sect. 3) also play a role. As for the percentage of large droplet, even at the highest pressure, the $x_{90,3}$ presents values around 500–1000 μm, which is significantly higher than the 200–300 μm that was seen at lower viscosities [15]. Furthermore, for most industrial applications, such as the spray drying of milk products, coffee, pigments and even ceramics, the expected droplet sizes tend to be a maximum of 200–400 μm [36]. This indicates that the large droplet sizes evidenced in Fig. 7 might cause issues if the ACLR nozzle were simply implemented, as is, in a spray dryer. Nonetheless, there are also two important caveats to add here. First, it should be noted that the current operating pressures, and ALRs, of the ACLR nozzle are comparatively low to commercially available nozzles. Therefore, increasing the atomization pressure could be considered to further reduce the $x_{90,3}$. Besides simply increasing the pressure, another option would be to improve the nozzle geometrical design, to reduce the flow instabilities of the annular flow. Second, it should also be considered that the increase in feed dry-matter content that could possibly be achieved with the ACLR nozzle would impact overall the process and its requirements. Most relevant, it would reduce the skin formation and general drying time of the droplets inside the spray tower [37]. This means that one would have to consider the possible adjustments in operating conditions and general configuration of the drying tower, before one can determine the effect of the large droplet sizes on wall deposition, caking and particle agglomeration.

On a separate matter, the rapid measurements of the DSD, at 10 kHz, were carried out. As a reminder, the objective of the rapid measurements was to more accurately determine the temporal variations of the characteristic droplet sizes, that is, the percentile droplet sizes and the SMD. Unfortunately, it was not possible to perform the rapid measurements for all the maltodextrin solutions. Namely, not enough data could be collected for the 57 % wt. solution. The reason may be that the spray pattern that forms at the highest viscosity is not uniform, at least with the pressures that can be achieved with the current experimental setup. To exemplify this, Fig. 8 shows a comparison of the spray cone pattern of

the 54 % and 57 % wt. solutions at the same pressure. The photos in Fig. 8 were not taken with the same high-speed camera described in Section 4.1, but instead with a standard Canon EOS 100D (Canon Deutschland GmbH, Krefeld, Germany), with a exposure time of 40 μm. The reason for this was the field of view of the standard camera was much wider than that of the high-speed one, allowing us to capture a larger section of the spray cone. As one can see, the spray tends to develop a much more concentrated one-sided jet and a sparser surrounding cone for 57 %. The jet itself is not stationary, and forms randomly in any direction, but the laser itself is stationary. This was not a problem for the low-frequency measurements, since the droplet sizes were measured every second over 2 min. In this case, the laser might still be able to collect enough diffraction data of the one-sided jet to produce a DSD. With the rapid measurements, the droplet sizes were measured every 0.1 ms over only a second, so no reliable data could be produced. Future work might need to expand the measuring time, which might allow enough data to be collected.

Because of the aforementioned limitation, only the rapid DSD measurements for the 52 % wt. and 54 % wt. solutions are shown in Fig. 9. To summarize the data, the figure shows the averaged values from the percentiles of the 10,000 DSDs that were measured for each maltodextrin solution at the different ALRs. In general, the percentile droplet sizes decrease with ALR. This is similar to the trend observed for the lamella thickness in Fig. 5. Additionally, in the range of ALR where there is an overlap, the $x_{50,3}$ of both maltodextrin solutions have similar values, in spite of the difference in their viscosities. One outlier value seems to be the lowest ALR of the 52 % wt., which shows both lower $x_{50,3}$ and $x_{90,3}$ than the rest of measurements. Given that this was not observed in the DSDs shown in Fig. 7a, it might be a consequence of the short measuring time of the rapid measurements. Longer measurements would have to be conducted at 10 kHz to validate the trends observed here. As also noticed for the DSDs in Fig 7, the large $x_{90,3}$ values show that higher ALRs or a geometrical improvement are needed to achieve droplet sizes that are appropriate for spray drying processes.

To further characterize the droplet sizes obtained from the spray, we calculated the Sauter and volumetric mean diameters for the DSDs shown in Fig. 9. The volumetric mean diameter ($\bar{x}_3$) is also known as the De Brouckere mean [38]. Additionally, we calculated the range and span of the DSDs to characterize their width. As the range, we simply calculated the difference between the $x_{90,3}$ and $x_{10,3}$. The span is this range divided by the $x_{50,3}$ [38]. All these statistics are shown in Table 4. In general, the mean values and the range decrease consistently with

higher ALRs. The outlier behavior observed for 52 % wt. MD at the lowest ALR, which was observed in Fig. 9, can also be seen here. Comparing between the different MD mass fractions, similar ALRs lead to different mean values, so the effect of the feed viscosity cannot be disregarded. As for the span, it is difficult to distinguish a consistent trend.

The expected mean values for pneumatic nozzles range reportedly between 30 and 150 μm [11]. The SMD seems to lie within this range for the MD solutions analyzed, but the De Broucker means show much larger droplet sizes. This is because a volumetric mean is more biased towards the large droplets that form part of the spray. Nonetheless, it is promising to see that the mean values, as well as the $x_{90,3}$, can all be strongly reduced even at ALRs of only 0.23 (for the 52 % wt. solution) and 0.42 (for the 54 % wt. solution). This shows that it might be possible to further narrow the DSDs to desirable conditions while still remaining at ALR < 1, which highlights the potential of the ACLR nozzle is for high-viscosity application.

2.4. Correlation between lamella thickness, spray cone and droplet size variations

The connection between the internal and external instabilities was investigated by analyzing the flow pattern inside and outside the nozzle. Fig. 10 shows an example of these flow patterns, at two different pressures, for the 54 % wt. MD solution. At low pressures and ALRs (see 0.2 MPa in Fig. 10) the internal flow resembles a slug flow, with no continuous air core, but rather air pockets intermittently flowing through the outlet channel. The effect of the internal slug flow on the external flow is also evident in Fig. 10. It causes the liquid lamella outside the nozzle to intermittently burst, followed by short interruptions of the liquid film. This pulsating behavior is not desirable in regards to achieving a stable atomization. In comparison, when operating at higher pressures and ALRs (see 0.7 MPa in Fig. 10), an annular flow can be achieved inside the nozzle, which also corresponds to a continuous spray cone forming outside the nozzle. This correlation between the internal and external flows, where an intermittent plug flow causes a pulsating spray cone to appear, while a stable annular flow leads to a more stable and uniform spray cone, has been seen before for other internal-mixing nozzles, such as the effervescent nozzle described by Lörcher and Mewes [39]. It should be mentioned again that, even when talking about "high" pressures and ALRs, the 0.7 MPa and ALR of 0.42 are very low in comparison to the operating conditions of pressure swirls (5–25 MPa [7]), which would not be able to handle these viscosities anyway, or airblast nozzles, which require ALRs between 1 and 15 [35].

For a more quantitative analysis of the flow and spray instabilities, the FFT analysis was used to determine the dominant oscillation frequencies of our parameters of interest: the lamella thickness, the spray angle, as well as the $x_{50,3}$ and $x_{90,3}$ of the DSD. These frequencies are shown in Table 5. As a reminder from what was discussed in Section 4.4, we classified the dominant frequencies according to how close they were to the lamella thickness frequencies. Frequencies within ±50 Hz of the lamella thickness values were considered matching and are highlighted in green and underlined. Frequencies within ±200 Hz of the lamella thickness values were considered similar and are highlighted in orange and italicized. Comparing the frequencies, it is evident that the instabilities of the spray cone, represented by the spray angle, match very consistently with the lamella thickness instabilities. This corresponds with the qualitative spray observation shown in Fig. 10 and serves as indication that the internal and spray cone instabilities are well correlated. For the droplet sizes, the correlation is not consistent, although around 60 % of the calculated frequencies of the $x_{50,3}$ match, or are at least similar to the lamella thickness instabilities. It should be kept in mind, that the calculated frequencies could range anywhere between 1 and 5000 Hz, so the fact that they are within the same 5 % bracket (± 200 Hz) in more than half of the analyzed cases can indicate some

connection between the internal and the droplet sizes instabilities. This is reinforced by Figs. 4 and 8, which show that both the lamella thickness and $x_{50,3}$ decrease similarly with the ALR.

3. Conclusions

The performance of the ACLR nozzle was successfully evaluated for maltodextrin solutions with viscosities up to 3 Pa•s and dry-matter fractions up to 57 % wt., focusing on three parameters as criteria: the internal lamella thickness, the spray cone angle, and the DSD. For the internal lamella, both its thickness and variation range decrease markedly with higher ALR. In fact, it seems that similar ALRs lead to similar thickness values, regardless of the liquid viscosity, which is promising for a further increase of the dry-matter concentration and further process intensification. However, one has to deal with challenges for stably pumping the feed at these high viscosities.

With regards to the spray cone, there was no consistent correlation between the ALR and the measured spray angles, at least within the range of pressures analyzed. The values for the 52 % wt. solution were an exception, as they showed a slight but consistent increase with higher ALRs. The spray angle ranged between 20 and 30°. This is much smaller than the values observed before for lower viscosities, which ranged between 40 and 70°.

On the topic of the DSD, it is already a significant achievement that the ACLR can atomize liquids with viscosities up to 3 Pa•s at pressures of barely 0.7 MPa and ALRs below 1. This is very small in comparison to the pressure requirements of pressure swirls and air flow requirements of external-mixing nozzles. However, the atomization presents a fraction of large droplets, which leads to $x_{90,3}$ values above 500 μm even at 0.7 MPa. These droplets are outside of the size range expected in industrial applications. For the foreseeable application of the ACLR nozzle, future work should characterize the DSD at higher ALRs and pressures. It might also be necessary to improve the nozzle geometrical design. The effect of the high dry-matter concentrations on the particle morphology and the drying kinetics, e.g., the skin formation, and general drying time, should also be analyzed.

Finally, the temporal instabilities of the internal lamella and the spray cone could be correlated with each other, by evidencing that their dominant frequencies consistently match. In contrast, no consistent correlation could be evidenced with the droplet sizes. However, the $x_{50,3}$ shared similar frequencies with the internal lamella in around 60 % of the analyzed cases. Additionally, both the lamella thickness and the droplet sizes decrease similarly with increasing ALR. These two facts are indications that it should still hold true that reducing the range of variation of the lamella also reduce the width and temporal unsteadiness of the DSD. This means that future studies, which may aim to improve the stability of the ACLR nozzle, could simply focus on one of the three parameters (lamella thickness, spray cone angle or DSD), and they can reasonably expect that the others will also decrease accordingly.

CRediT authorship contribution statement

Miguel Ángel Ballesteros Martínez: Writing – original draft, Investigation, Software, Formal analysis, Data curation. **Prithika Roy:** Writing – original draft, Writing – review & editing, Software, Formal analysis. **Juan Nicolás Solano Alarcón:** Writing – review & editing, Investigation, Data curation. **Volker Gaukel:** Writing – review & editing, Resources, Project administration, Funding acquisition, Formal analysis.

Declaration of competing interest

The authors declare the following financial interests/personal relationships which may be considered as potential competing interests:

Miguel Angel Ballesteros Martinez reports financial support was provided by Deutsche Akademische Austauschdienst (DAAD). Volker

Appendix A. Fitting parameters for non-Newtonian rheological models

The fitting parameters are shown in Table 6 for the Cross model and in Table 7 for the CY model. In all cases, the η_∞ was set to 0. In general, the parameters highlight that the increase in the dry-matter content correlates to higher viscosity (see the zero viscosity) and a stronger shear-thinning effect. This shear thinning can be noticed in the parameter m approaching unity, for the Cross model, or the power index n consistently decreasing, for the CY model. Concerning the CY model, the deviation observed for the solutions with lower MD content can be noticed in the relaxation time λ and the parameter a, which are much larger than the ones of the other mixtures.

Appendix B. Distance between nozzle exit and DSD measurement

When determining the DSD, it is important to ensure that the measurement is conducted at enough distance from the nozzle outlet, so that the primary atomization process has mostly already taken place. Additionally, the laser diffraction principle, used to measure the DSD in this study, is based on the assumption that the liquid parts that cross the laser are mostly spherical [27] and not irregular ligaments. This implies that the ligaments must have been broken up and that surface tension forces have prevailed and made the ligament spherical. The length required for this to happen is known to depend both on the liquid viscosity as well as the ALR at which the pneumatic nozzle is operating [40].

With this in mind, it is clear that distance at which we were measuring the DSD was an important decision. The methodology we utilized to measure the DSD was based on a previous study carried out on the ACLR nozzle by Wittner et al. [25], which utilized a vertical distance of 25 cm between the nozzle and the laser spectrometer. Nonetheless, two differences with this study had to be taken into consideration here. First, Wittner et al. only analyzed MD solution viscosities of up to 0.39 Pa•s, while the viscosity of the mixtures used in this study reaches 3 Pa•s (see Fig. 1). Second, they reached ALRs only up to 0.3, while in our study the maximum ALRs range between 0.23–0.77 depending on the maltodextrin concentration (see Table 3). Given that the higher viscosities and higher ALRs have opposite effects on the breakup length required, it was not evident if and how the measuring distance should be changed.

To clarify that, we recorded the liquid breakup outside the nozzle, utilizing the 54 % wt. MD solution, at the lowest and highest pressures: 0.2 and 0.7 MPa. For that purpose, we used a standard Canon EOS 100D, with an exposure time of 17 μm. This standard camera was used instead of the high-speed one, described in Section 4.1, because the standard camera had a wider field of view, allowing us to capture a larger section of the spray cone. For the two pressures analyzed, the spray patterns observed up to 10 cm below the nozzle exit are shown in Fig. 11. As it can be noticed, the liquid seems to have broken up mostly by this point, even at 0.2 MPa. That means that the large ligaments near the nozzle, observed in Figs. 3 and 10, should have enough time to break up into more spherical droplets before they reach the laser, even if it were placed as the same distance as in Wittner et al. [25]. Unfortunately, we could not directly confirm that assumption, because we could not record a field of view wide enough to cover the entire spray cone, with a low enough exposure time and high enough resolution to capture the fine liquid ligaments and droplets. Because of that limitation, we decided to increase the laser distance to the maximum possible in our spray cabin setup, namely, 35 cm. With that safety measure, we were mostly certain that the DSD measurements were reliable for the purposes of this study.

Data availability

Data will be made available on request.

References

[1] M. Fox, C. Akkerman, H. Straatsma, P. Jong, Energy reduction by high dry matter concentration and drying, New Food 6 (2010) 60–62.

[2] D. Daković, M. Kljajić, N. Milivojević, D. Doder, A.S. Anđelković, Review of energy-related machine learning applications in drying processes, Energies 17 (2023) 224, https://doi.org/10.3390/en17010224.

[3] I.C. Claussen, S. Sannan, M. Bantle, M. Lauermann, V. Wilk, *Specification of performance indicators and validation requirements, EU Project No.: 723576 "DryFiciency Waste Heat Recovery in Industrial Drying Processes"*; European Union, 2021. https://dryficiency.eu/wp-content/uploads/2021/08/D1_2_Performance-i ndicators-and-validation-requirements_Update-Scanship.pdf (accessed March 4, 2024).

[4] J.C. Atuonwu, X. Jin, G. Van Straten, H.C.V. Deventer Antonius, J.B. Van Boxtel, Reducing energy consumption in food drying: opportunities in desiccant adsorption and other dehumidification strategies, Procedia Food Sci. 1 (2011) 1799–1805, https://doi.org/10.1016/j.profoo.2011.09.264.

[5] M.O. Wittner, H.P. Karbstein, V. Gaukel, Energy efficient spray drying by increased feed dry matter content: investigations on the applicability of Air-core-liquid-ring atomization on pilot scale, Drying Technol. 38 (2020) 1323–1331, https://doi.org/10.1080/07373937.2019.1635616.

[6] P. Stähle, V. Gaukel, H.P. Schuchmann, Comparison of an effervescent nozzle and a proposed air-core-liquid-ring (ACLR) nozzle for atomization of viscous food liquids at low air consumption, J. Food Process Eng. 40 (2017) 12268, https://doi.org/10.1111/jfpe.12268.

[7] M.A. Ballesteros Martínez, V. Gaukel, Using computation fluid dynamics to determine oil droplet breakup parameters during emulsion atomization with pressure swirl nozzles, Fluids 8 (2023) 277, https://doi.org/10.3390/fluids8100277.

[8] G. Wozniak, Technische zerstäuber, in: G. Wozniak (Ed.), *Zerstäubungstechnik*, Springer Berlin Heidelberg, Berlin, Heidelberg, 2003: pp. 57–87. https://doi.org/10.1007/978-3-642-55835-1_5.

[9] F.A. Hammad, K. Sun, J. Jedelsky, T. Wang, The effect of geometrical, operational, mixing methods, and rheological parameters on discharge coefficients of internal-mixing twin-fluid atomizers, Processes 8 (2020) 563, https://doi.org/10.3390/pr8050563.

[10] P. Stähle, J. Schröder, A. Kleinhans, H.P. Schuchmann, V. Gaukel, Effervescent atomization: a new atomizing technique for the energy-efficient spray drying of food liquids with high viscosity, Int. Dairy Magazine 8 (2013) 26–28, https://doi.org/10.5445/IR/1000051535.

[11] C. Anandharamakrishnan, S.P. Ishwarya, *Spray drying technique for food ingredient encapsulation*, Wiley-Blackwell, IFT Press, Chichester, West Sussex ; Hoboken, NJ, 2015.

[12] G.V. Barbosa-Cánovas, E. Ortega-Rivas, P. Juliano, H. Yan, *Food Powders: Physical Properties, Processing, and Functionality*, Springer US, Boston, MA, 2005. https://doi.org/10.1007/0-387-27613-0_11.

[13] M.O. Wittner, M.A. Ballesteros, F.J. Link, H.P. Karbstein, V. Gaukel, Air-core–Liquid-ring (ACLR) atomization part II: influence of process parameters on the stability of internal liquid film thickness and resulting spray droplet sizes, processes 7 (2019) 616. https://doi.org/10.3390/pr7090616.

[14] A. Kleinhans, J. Schröder, P. Stähle, V. Gaukel, H.P. Schuchmann, Investigation on the usage of effervescent atomization for spraying and spray drying of rheological complex food liquids and on the resulting particle and product properties, in: U. Fritsching (Ed.), Process-Spray: Functional Particles Produced in Spray Processes, Springer International Publishing, Cham, Switzerland, 2016, pp. 843–902.

[15] M.A. Ballesteros Martínez, V. Gaukel, Understanding the operating limitations of an internal-mixing air-core-liquid-ring (ACLR) nozzle for process intensification in spray drying, Dry. Technol. (2024) 1–8, https://doi.org/10.1080/07373937.2024.2328300.

[16] P.J. Carreau, Rheological equations from molecular network theories, Trans. Soc. Rheol. 16 (1972) 99–127, https://doi.org/10.1122/1.549276.

[17] K. Yasuda, R.C. Armstrong, R.E. Cohen, Shear flow properties of concentrated solutions of linear and star branched polystyrenes, Rheol. Acta 20 (1981) 163–178, https://doi.org/10.1007/BF01513059.

[18] M.M. Cross, Rheology of non-newtonian fluids: a new flow equation for pseudoplastic systems, J. Colloid Sci. 20 (1965) 417–437, https://doi.org/10.1016/0095-8522(65)90022-X.

[19] M.P. Escudier, I.W. Gouldson, A.S. Pereira, F.T. Pinho, R.J. Poole, On the reproducibility of the rheology of shear-thinning liquids, J. Nonnewton Fluid Mech. 97 (2001) 99–124, https://doi.org/10.1016/S0377-0257(00)00178-6.

[20] Siemens Industries Digital Software, Simcenter STAR-CCM+ User Guide, version 2206, (2022). https://plm.sw.siemens.com/en-US/simcenter/fluids-thermal-simulation/star-ccm/.

[21] ANSYS, Inc., Ansys Fluent Theory Guide, Release 2019 R3, (2019).

[22] M.A. Ballesteros Martínez, D. Becerra, V. Gaukel, Modelling the flow conditions and primary atomization of an air-core-liquid-ring (ACLR) atomizer using a coupled eulerian–Lagrangian approach, Flow Turbulence Combust. 113 (2024) 437–458, https://doi.org/10.1007/s10494-024-00555-1.

[23] M.A. Ballesteros Martínez, V. Gaukel, Time-averaged analysis and numerical modelling of the behavior of the multiphase flow and liquid lamella thickness inside an internal-mixing ACLR nozzle, Flow Turbulence Combust. 110 (2023) 601–628, https://doi.org/10.1007/s10494-023-00406-5.

[24] J. Schröder, A. Gunther, K.-E. Wirth, H.P. Schuchmann, V. Gaukel, Effervescent atomization of polyvinylpyrrolidone solutions: influence of liquid properties and atomizer geometry on liquid breakup and spray characteristics, Atomiz Spr. 23 (2013) 1–23, https://doi.org/10.1615/AtomizSpr.2013005849.

[25] M.O. Wittner, H.P. Karbstein, V. Gaukel, Air-core-liquid-ring (ACLR) atomization: influences of gas pressure and atomizer scale up on atomization efficiency, processes 7 (2019) 139. https://doi.org/10.3390/pr7030139.

[26] A. Mescher, P. Walzel, Störeinfluss durch Schlieren bei der tropfengrößenmessung an Zweistoffdüsen durch laserbeugungsspektrometrie, Chem. Ing. Tech. 82 (2010) 717–722. https://doi.org/10.1002/cite.200900166.

[27] M.O. Wittner, H. Karbstein, V. Gaukel, Pneumatic atomization: beam-steering correction in laser diffraction measurements of spray droplet size distributions, Appl. Sci. 8 (2018) 1738, https://doi.org/10.3390/app8101738.

[28] M.S. Reis, P.M. Saraiva, B.R. Bakshi, Denoising and Signal-to-Noise Ratio Enhancement: Wavelet Transform and Fourier Transform, in: Comprehensive Chemometrics, Elsevier, 2009: pp. 25–55. https://doi.org/10.1016/B978-044452701-1.00099-5.

[29] L. Sevgi, Numerical fourier transforms: DFT and FFT, IEEE Antennas Propag. Mag. 49 (2007) 238–243. https://doi.org/10.1109/MAP.2007.4293982.

[30] S.L. Gjelstrup, FFT analysis (Fast Fourier Transform): the ultimate guide to frequency analysis, (2023). https://dewesoft.com/blog/guide-to-fft-analysis (accessed January 29, 2025).

[31] J.W. Cooley, J.W. Tukey, An algorithm for the machine calculation of complex fourier series, Math. Comp. 19 (1965) 297–301, https://doi.org/10.1090/S0025-5718-1965-0178586-1.

[32] S.M. Kuo, B.H. Lee, Real-time digital signal processing: implementations, applications, and experiments with the TMS320C55X, Wiley, Chichester, West Sussex, 2001.

[33] A.H. Lefebvre, V.G. McDonell, *Atomization and sprays*, 2nd ed., CRC Press, Boca Raton; London; New York, 2017. https://doi.org/10.1201/9781315120911.

[34] M.M. Tareq, R.A. Dafsari, S. Jung, J. Lee, Effect of the physical properties of liquid and ALR on the spray characteristics of a pre-filming airblast nozzle, Int. J. Multiphase Flow 126 (2020) 103240, https://doi.org/10.1016/j.ijmultiphaseflow.2020.103240.

[35] A. Mansour, N. Chigier, Air-blast atomization of non-Newtonian liquids, J. Nonnewton Fluid Mech. 58 (1995) 161–194, https://doi.org/10.1016/0377-0257(95)01356-Z.

[36] I. Filková, A.S. Mujumdar, Industrial spray drying systems, in: Arun S. Mujumdar (Ed.), *Handbook of Industrial Drying*, 4th ed., CRC Press, 2014: pp. 263–307.

[37] E.M. Both, S.M.B. Tersteeg, R.M. Boom, M.A.I. Schutyser, Drying kinetics and viscoelastic properties of concentrated thin films as a model system for spray drying, Colloids Surfaces A: Physicochem. Eng. Aspect 585 (2020) 124075, https://doi.org/10.1016/j.colsurfa.2019.124075.

[38] S. Fan, S. Chen, Z. Wu, S. Wu, Y. Chen, D. Liu, Y. Yao, J. Huang, Analysis of droplet size distribution and selection of spray parameters based on the fractal theory, J. Clean. Prod. 371 (2022) 133315, https://doi.org/10.1016/j.jclepro.2022.133315.

[39] M. Lörcher, D. Mewes, Zerstäuben durch kritisches ausströmen eines Wasser/Luft-Gemisches aus einer innenmischenden Zweistoffdüse, Chem. Ing. Tech. 74 (2002) 280–285. https://doi.org/10.1002/1522-2640(200203)74:3<280::AID-CITE280>3.0.CO;2-N.

[40] M. Roudini, G. Wozniak, Experimental investigation of spray characteristics of pre-filming air-blast atomizers II – Influence of liquid properties, JAFM 13 (2020) 679–691, https://doi.org/10.29252/jafm.13.02.30336.